Research Square

Preprints are preliminary reports that have not undergone peer review.
They should not be considered conclusive, used to inform clinical practice,
or referenced by the media as validated information.

A Wearable Patch with Iontronic Linear Sensing and Mechanically Compliant Wireless Readout for Physiological Signals

Zhuang Su
Xidian University
Chengxi Guo
Xidian University
Linxuan Zhou
Xidian University
Ke Liu
Xidian University
Xi Wang
Xidian University
Ran Zhang
Xidian University
Bo Teng
Xidian University
Hongcheng Xu
Xi'an Jiaotong University
Chuan Fei Guo
Southern University of Science and Technology
Weidong Wang
Xidian University
Ningning Bai
nnbai@xidian.edu.cn

Xidian University

Article

Keywords: flexible wearable patch, iontronic pressure sensor, wide linear range, mechanically compliant electronics, physiological monitoring

Posted Date: November 13th, 2026

DOI: https://doi.org/10.21203/rs.3.rs-11075373/v1

License: This work is licensed under a Creative Commons Attribution 4.0 International License.
Read Full License

Additional Declarations: No competing interests reported.

A Wearable Patch with Iontronic Linear Sensing and Mechanically Compliant Wireless Readout for Physiological Signals

Zhuang Su[#,1], Chengxi Guo [#,1], Linxuan Zhou [1], Ke Liu [1], Xi Wang[1], Ran Zhang[1], Bo Teng[1], Hongcheng Xu[3], Chuan Fei Guo[4], Weidong Wang[*,1,2], Ningning Bai[*,1,2]

[1]School of Mechano-Electronic Engineering, Xidian University, Xi'an 710071, P.R. China

[2]State Key Laboratory of Electromechanical Integrated Manufacturing of High-Performance Electronic Equipment, Xi'an 710071, P.R. China

[3]School of Instrument Science and Technology, Xi'an Jiaotong University, Xi'an 710049, P.R. China

[4]Department of Materials Science and Engineering, Southern University of Science and Technology, Shenzhen 518055, P.R. China

[#] These authors contributed equally

[*] Corresponding authors:

Weidong Wang: e-mail: wangwd@mail.xidian.edu.cn

Ningning Bai: e-mail: nnbai@xidian.edu.cn

Abstract

Wearable wireless sensing patches enable continuous monitoring of physiological mechanical signals in clinical and daily settings. However, they often suffer from limited linearity and motion-induced drift due to deformation during body movement during daily activities. We report an integrated, flexible, and miniaturized wearable patch (FMWP) that couples an iontronic pressure sensor with a wireless readout circuit for skin-mounted monitoring. The sensor employs a CNT-doped ionic film with double-sided irregular microstructures that deform progressively, producing a nearly proportional increase in contact area and hybrid ion-electron transport, thereby enabling iontronic capacitive sensing with a high sensitivity (13.5 kPa^{-1}) and wide linear range (2−450 kPa, $R^2 \sim 0.999$). A quadrant-grid spacer suppresses preload contact and stabilizes the baseline capacitance, achieving fast dynamic response (6 ms response, 9 ms relaxation) and durability over 5,000 loading cycles. The backend uses rigid electronic islands interconnected by serpentine copper traces to mechanically limit deformation around functional components and suppress deformation-induced electrical variations, while a patterned porous fiber layer provides breathability and reliable, removable skin adhesion. The FMWP enables real-time, smartphone-based multi-parameter physiological signal monitoring, including pulse, respiration, cardiac microvibrations, and swallowing, offering a practical platform for long-term health assessment.

Keywords: flexible wearable patch; iontronic pressure sensor; wide linear range; mechanically compliant electronics; physiological monitoring

Introduction

Wearable devices act as a direct interface between the human body and digital systems, transforming health monitoring and enabling more natural intelligent human–machine interaction.[1–3] Compared with rigid platforms, skin-mounted soft systems maintain conformal contact during motion, which reduces motion artifacts in long-term monitoring of pulse,[4] respiratory rate,[5] and heart rate.[6] For practical use, the sensing front-end and signal-acquisition electronics need to work reliably together under skin deformation..[7,8]

At the sensing front-end, flexible pressure sensors need to balance high sensitivity with a wide linear working range.[9-11] High sensitivity is crucial for detecting weak physiological stimuli, whereas a broad linear range simplifies circuit design, reducing the complexity of readout electronics and improving system robustness.[12] Recently, flexible iontronic pressure sensors have been developed that replace the dielectric layer with an ionic film and form electric double layers (EDLs) with a supercapacitive interface at the electrode/ionic film interface,[13-15] thereby increasing the capacitance density and signal amplitude compared with conventional pressure sensors. Iontronic devices with flat ionic films or electrodes often show low sensitivity in the medium- and high-pressure ranges because the contact area (A) at the sensing interface changes very little under compression. Introducing regular microstructured arrays[16], such as pyramids,[17,18] pillars,[19,20] or hemispheres,[21,22] into iontronic devices can enhance sensitivity by enabling a variable A at the sensing interface. However, these sensors commonly exhibit nonlinear responses at high pressures because geometric stiffening

saturates both deformation and the effective A, making it difficult to simultaneously achieve high sensitivity and a wide linear range.[23,24] Several strategies, including multilayer,[25,26] interlocked,[27] and foam/porous structures[28–30] have been used to enhance compressibility of the iontronic interface, promoting an approximately linear increase in A with pressure and thereby improving sensitivity while extending the linear range. Nevertheless, these structures often rely on complex and costly micro/nano fabrication processes, such as high-resolution 3D printing[31,32] and laser engraving,[33,34] which hinder large-area manufacturing and system integration.

Beyond the sensing front end, the readout electronics introduce another constraint. Rigid printed circuit boards provide stable electrical connections but do not conform to skin. When the circuit deforms with the body, parasitic capacitance and interconnect resistance can change the sensor signal.[35,36] To mitigate these issues, wearable systems are gradually shifting from rigid configurations toward semi-flexible or fully flexible substrates based on elastomeric hydrogels,[37–39] and textiles.[40–42] Elastomeric hydrogel-based substrates offer favorable mechanical robustness, and fatigue resistance, but limited breathability can cause moisture buildup, leading to discomfort during prolonged wear. Textile substrates conform well to highly curved regions such as joints and offer good breathability, but their inherently discrete conductive networks significantly increase bulk resistance, which is unfavorable for accurate acquisition of weak physiological signals. In addition, integration of multiple functional modules on textiles often requires stacking multiple fabric layers, making system miniaturization and optimization more difficult. Together, these limitations make it difficult to build

compact wearable systems that maintain stable sensing and readout during deformation. Reliable physiological monitoring therefore requires a sensor with high sensitivity and a wide linear range. And, the readout circuit should also remain electrically stable under deformation without introducing motion-related artifacts.

In this work, we present a portable, flexible and miniaturized wearable patch (FMWP) that integrates an iontronic pressure sensor with linear response and a flexible wireless acquisition module into a skin-mounted system. The patch combines breathable thermoplastic polyurethane (TPU) fiber and Ecoflex encapsulation, weighing about 3.2 g with an overall thickness of about 2.8 mm. The sensor employs carbon nanotubes (CNTs) doped ionic film engineering with a double-sided irregular structure (DSIS) that enables near linear contact area evolution and mixed ion-electron transport, delivering high linearity ($R^2 \approx 0.999$), high sensitivity (13.5 kPa^{-1}) over a wide linear range up to 450 kPa. The backend uses rigid electronic islands bridged by compliant interconnects to preserve electrical stability under deformation. The system supports real-time Bluetooth monitoring of pulse, respiration, and cardiac microvibrations via a smartphone app.

Results

Design of the FMWP

The FMWP is designed for continuous, skin-mounted monitoring of physiological mechanical signals while maintaining comfort during prolonged attachment. As shown in **Fig. 1a**, the patch (size: 5 cm × 2.6 cm × 2.8 mm) integrates an iontronic sensing module, an onboard data processing module, and a Bluetooth transmission module.

Mechanical signatures from pulse, cardiac microvibration, respiration, and swallowing are acquired at the sensing interface, processed locally, then wirelessly transmitted to a smartphone for real-time waveform display.

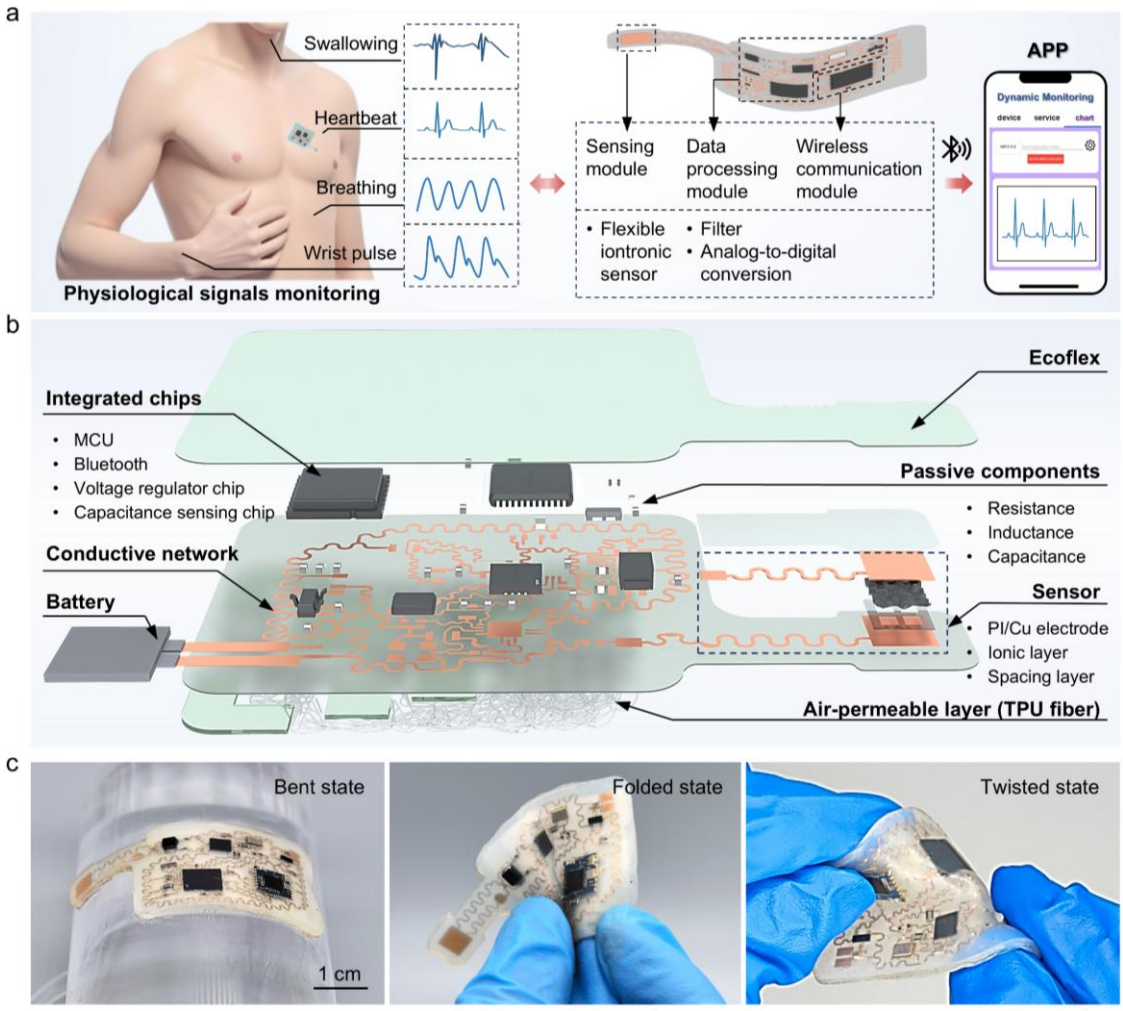


Fig. 1 Overview and design of the flexible, miniaturized wearable patch (FMWP). a System level schematic of the FMWP. Swallowing, cardiac, respiratory, and pulse signals are acquired by the sensing module, conditioned and processed, wirelessly transmitted, and visualized in real-time as waveforms in a mobile app for multi-parameter physiological monitoring. **b** Exploded view of the fully integrated FMWP, including the sensing front end and the backend circuitry. **c** Photographs showing the conformability of the FMWP in the bent (conforming to a cylindrical surface), folded and twisted states.

To accommodate skin deformation, the patch adopts an island–bridge layout, with rigid

components mounted on functional islands linked by serpentine interconnects (**Fig. 1b**).[43] The sensing element is positioned at one end of the patch, spatially separated from the main readout and communication circuitry. The interconnects provide mechanical compliance between the component islands and the sensing region, while encapsulation protects the components and electrical connections. The skin-contact interface is designed to provide local adhesion while allowing water vapor transport during prolonged wear. The assembled patch conforms to a cylindrical surface and can be folded and twisted (**Fig. 1c**), demonstrating mechanical flexibility suitable for skin-mounted physiological monitoring.

Structural Design, Sensing Mechanism, And Sensing Performance of the DSIS-based Iontronic Pressure Sensor

Accurate epidermal monitoring requires a pressure sensor that resolves subtle physiological stimuli while maintaining linear response under larger transient loads. In iontronic pressure sensors, signal transduction is dominated by EDL capacitance at the electrode and ionic film interfaces, where the pressure dependent evolution of real contact area strongly determines output. We therefore tailored the interfacial microstructure and the ionic layer composition to regulate A under compression while sustaining low impedance for stable capacitive readout.

To regulate the increase in real contact area across different pressure regimes, we designed three interfacial microstructures: a single-sided regular structure, a single-sided irregular structure, and a double-sided irregular structure (DSIS). Finite-element

analysis (FEA) was used to compare their deformation and contact-area responses under compression **(Fig. 2a).** Here, A_0 denotes the initial real contact area at nominal zero load, and $\Delta A = A - A_0$ is the pressure-induced increase in contact area. In the regular array, asperities of identical geometry deform simultaneously, causing a rapid increase in structural stiffness and early saturation of lateral expansion. Consequently, ΔA increases more slowly at intermediate-to-high pressures, and the ΔA–P relationship deviates from linearity (**Fig. 2b)**. In the single-sided irregular structure, asperities of different heights progressively engage as pressure increases, allowing the real contact area to continue increasing over a wider pressure interval and shifting the onset of saturation to higher pressures. DSIS introduces irregular microstructures on both surfaces, transforming one active interface into two cooperatively deforming interfaces. The two interfaces engage progressively and share the applied load, producing a normalized contact-area increase $\Delta A/A_0$ more than twice that of the single-sided irregular structure while maintaining an approximately proportional relationship with pressure over a broad range.

The DSIS ionic layer consists of a TPU incorporating 1-ethyl-3-methylimidazolium bis(trifluoromethanesulfonyl)imide ([EMIM][TFSI]) ionic liquid, with CNT additives to simultaneously tailor mechanical compliance and ionic/electronic transport.[44,45] The TPU matrix provides elasticity and robustness, whereas [EMIM][TFSI] and CNTs supply ion-electron conductance. CNT incorporation (1.7 wt%) increases the effective modulus, delays geometric saturation of the DSIS interface, and extends the quasi-linear pressure range. (**Fig. S1**). Impedance spectra further show that impedance

decreases with pressure for both CNT-doped and undoped films, while CNT-doped DSIS consistently exhibits lower resistance under load (**Fig. 2c)**, indicating a mixed ion electron transport network that reduces bulk and interfacial impedance and sustains signal magnitude at higher pressures. The DSIS ionic layers are fabricated by double-sided thermal imprinting of the TPU and [EMIM][TFSI] composite with CNTs using sandpaper templates (**Fig. S2)**. SEM images confirm hierarchical protrusions and microgrooves on both surfaces of the demolded film (**Fig. 2d and Fig. S3)**. PI/Cu films are laser cut into square-shaped electrodes, and the sensor is assembled by sandwiching the DSIS ionic layer between two electrodes in a vertical metal/ionic-layer/metal stack **(Fig. S4)**. Under bias, compression drives ions and electrons to accumulate within nanometer scale distances at both interfaces, forming EDLs that increase specific capacitance as contact area expands (**Fig. 2e and Fig. S5**).

Sensitivity was calculated from the slope of the normalized capacitance change versus pressure. A low and stable initial capacitance (C_0) increases the normalized response. Variations in packaging preload produce different degrees of initial contact between the electrode and ionic layer, causing C_0 to vary and reducing device-to-device consistency. We therefore introduced a spacer to maintain interfacial separation in the unloaded state, yielding a lower and more reproducible C_0. To quantify the influence of the spacer geometry on C_0 we compared three configurations: spacer-free, a solid square spacer, and a quadrant-grid spacer (**Fig. S6a**). Without a spacer, packaging-induced partial contact resulted in a C_0 of approximately 120 pF. A 10-μm-thick square polyethylene terephthalate (PET) spacer reduced C_0 to approximately 40 pF but

provided insufficient support in the central region. By contrast, the quadrant-grid spacer prevented unintended contact and reduced C_0 to ≤5 pF (**Fig. S6b**). During cyclic loading, the grid suppressed interfacial adhesion and allowed the ionic layer to separate rapidly from the electrodes upon unloading, thereby stabilizing the output baseline (**Fig. 2f**). Because the narrow grid ribs occupy only a small fraction of the electrode area, their effects on A and maximum capacitance are negligible. The quadrant-grid spacer was therefore used in all subsequent measurements.

As shown in **Fig. 2g**, the sensor based on the CNT-doped DSIS film exhibits an approximately linear response over a broad pressure range of 2–450 kPa, with a sensitivity of 13.5 kPa^{-1} and a fitting coefficient of $R^2 \sim 0.999$. By contrast, devices based on the CNT-free DSIS film show an earlier onset of nonlinearity at high pressures, supporting the role of CNT incorporation in amplifying the signal and extending the linear sensing range. Uniform 50 kPa pressure increments produce nearly constant changes in capacitance, yielding a highly linear response from 50 to 300 kPa. The small error bars further demonstrate good repeatability across the tested pressure levels. (**Fig. 2h**). The wide linear range results from the combined effects of DSIS and CNT incorporation. DSIS regulates contact-area evolution, while CNTs provide a mixed ion–electron transport pathway and reduce impedance at higher pressures.

In addition, the sensor exhibits negligible signal hysteresis. Capacitance–pressure curves measured at compression rates of 1, 5, and 10 $mm \cdot min^{-1}$ nearly overlap (**Fig. 2i**), and the capacitance closely follows the loading–unloading profile, indicating a stable and robust response. Response/relaxation time is another important parameter

for pressure sensors. Microstructured architectures have been proved to accelerate rebound and signal recovery by promoting rapid elastic energy storage and release.[27, 46, 47] Upon rapid step loading-unloading to 25 kPa (**Fig. 2j**), the device exhibits a 6 ms response time and a 9 ms relaxation time. This fast dynamic is enabled by rapid elastic recovery arising from the double-sided irregular microstructure and the introduced spacer, which collectively shortens the relaxation process. Under 5,000 compression–release cycles at a peak pressure of 130 kPa, the sensor maintains a consistent output without noticeable drift or fluctuation (**Fig. 2k)**, demonstrating the mechanical robustness required for stable, long-term operation. Moreover, the capture of motion signals and swallow-related vibrations further indicates that the sensing module can reliably capture target mechanical signals (**Fig. S7**), supporting subsequent miniaturization and patch integration.

Overall, the sensor incorporating the CNT-doped DSIS ionic film shows high sensitivity, a wide linear working range, fast dynamics, and good stability, providing a reliable front-end sensing module for integration into wearable patch systems in long-term pressure monitoring.

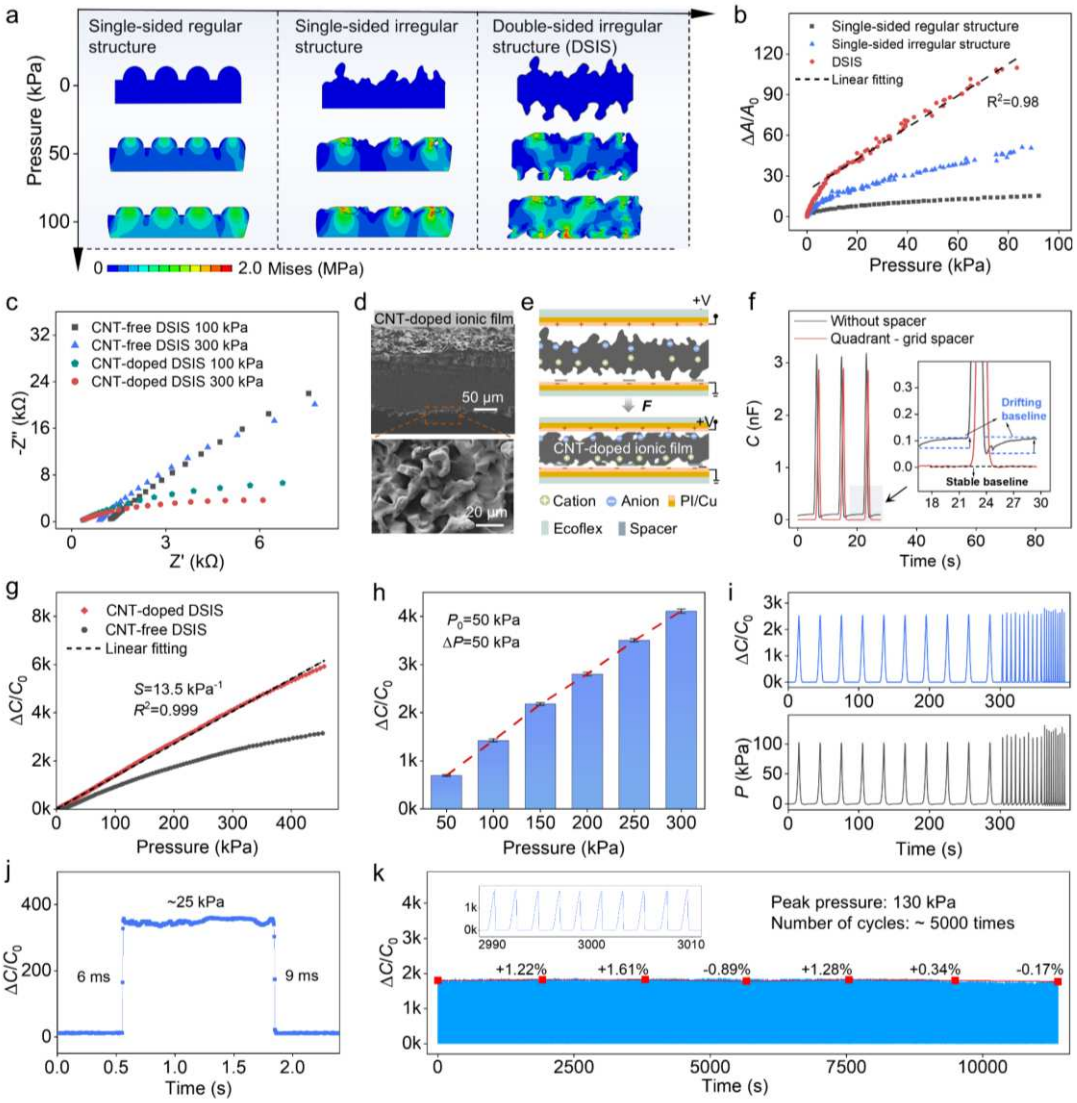


Fig. 2 Structural design and sensing mechanism, and sensing performance of the iontronic pressure sensor. a Stress distribution and compressive deformation from FEA for ionic layers with three microstructures under pressures up to 100 kPa: single-sided regular structure, single-sided irregular structure, and DSIS. **b** Normalized evolution of the contact area between the electrode and the ionic layer for the three configurations from 0 to 100 kPa. **c** Nyquist plots of CNT-free and CNT-doped DSIS measured under 100 kPa and 300 kPa pressure. **d** Cross-sectional and top-view SEM images of the CNT-doped DSIS ionic film at different magnifications. **e** Schematic illustration of the iontronic sensing mechanism before and after applying pressure. **f** Cycling response under repeated loading and unloading for sensors with no spacer and with the quadrant-grid spacer. **g** Capacitance change over pressures up to 450 kPa for sensors using DSIS ionic layers with and without CNTs. **h** Step response under pressures from 50 to 300 kPa in 50 kPa increments. Error bars

represent the standard deviation of multiple independent measurements. **i** Dynamic response at different compression rates. **j** Response and relaxation time at a pressure of ~ 25 kPa. **k** Working stability tested over 5,000 cycles under a high pressure of 130 kPa.

LC-resonant capacitance readout and system integration of the FMWP

Continuous monitoring on skin requires the capacitance response of the CNT-doped DSIS sensor to be converted, processed and transmitted by miniaturized electronics integrated in a mechanically compliant format. We developed a miniaturized system comprising an LC resonant front end, a frequency-to-digital converter, a microcontroller and a low-power Bluetooth module for wireless readout. (**Fig. 3a and Fig. S8**). At the readout front end, the iontronic pressure sensor is represented by a variable EDL capacitance C_{EDL}, which forms a parallel resonant circuit with an inductor (L), a fixed capacitor (C_{ref}) and the parasitic capacitance (C_{par}). The expressions for the total effective capacitance (C_{total}) and resonant frequency (f_s) are shown in **Fig. 3a**. Applied pressure enlarges the real contact area between the electrodes and ionic layer, increasing C_{EDL} and C_{total} and shifting f_s to a lower frequency. The FDC2214 interfaces with the LC resonant circuit and converts the resonance-frequency shift into a digital output. The microcontroller receives the digital output via I^2C, calculates the equivalent capacitance using the calibrated frequency-capacitance relation, and processes the data for transmission to a mobile device over Bluetooth (**Fig. S9**).

Implementing this readout scheme in a skin-mounted patch requires the circuit to accommodate deformation while maintaining electrical connections between rigid components. We therefore developed a rigid-soft integration approach using an island-bridge layout and patterned encapsulation to support rigid components locally while allowing the interconnects to deform. A PI/Cu laminate was laser-patterned to define the functional islands, contact pads and serpentine interconnects (**Fig. 3b**). The

patterned circuit was picked up with water-soluble tape and transferred onto partially cured Ecoflex (**Fig. S10 and Fig. 3c**). After the tape was dissolved, the electronic components were mounted on the functional islands and soldered. The iontronic sensor was soldered to enlarged contact pads on the readout circuit. An insulating coating was then sprayed over the assembled circuit, and Ecoflex was applied by spin coating to encapsulate the components, solder joints and metal traces. Finally, a patterned porous TPU fibrous layer was laminated to the skin-contact side of the encapsulated patch (**Fig. S11**). The completed flexible patch integrates iontronic sensing, data acquisition and processing, and Bluetooth communication (**Fig. 3d, left**).

The serpentine PI/Cu interconnects were designed to accommodate relative motion between the islands during bending, slight stretching and folding of the patch, while limiting strain in the rigid components and solder joints. Zero-ohm jumpers provided the required crossovers in the single-layer routing (**Fig. 3d, right**). The jumpers and their pads were positioned in regions expected to undergo little deformation. At the skin-contact surface, Ecoflex occupied the regions corresponding to the functional islands and the patch perimeter to provide local component support and edge adhesion (**Fig. S12**). The porous TPU covers the deformable regions containing the serpentine interconnects, allowing these regions to deform while providing a path for water-vapor transport.

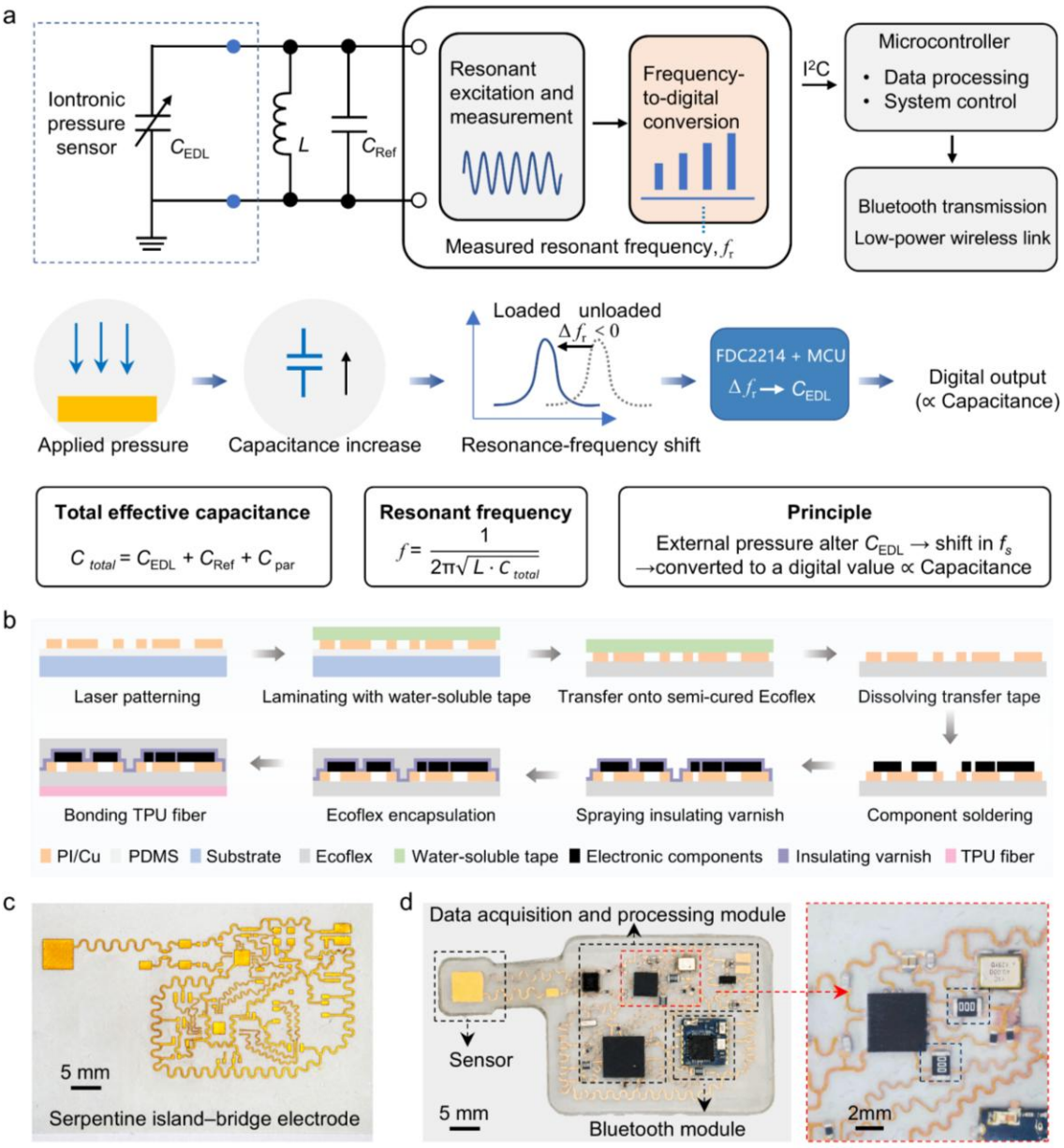


Fig. 3 LC-resonant capacitance readout and system integration of the FMWP. a Operating principle of the LC-resonant capacitance readout and wireless transmission pathway. **b** Schematic illustration of the FMWP fabrication process, including laser patterning and transfer of the PI/Cu circuit, electronic-component assembly and encapsulation, and integration of the porous TPU fiber layer. **c** Photograph of the laser-patterned serpentine island–bridge PI/Cu circuit layout before component assembly. **d** Photograph of the assembled FMWP, showing the iontronic pressure sensor, data-acquisition and processing module, and Bluetooth transmission module and microscopic optical photograph of TPU fiber.

Mechanical robustness, deformation-resilient signal acquisition, and skin-mounted reliability

The flexible circuit was evaluated under bending, twisting, and stretching. As shown in **Fig. 4a**, FEA was conducted to map the strain field in the FMWP under representative deformation modes, including conformal bending to a curved surface (bending radius r ~ 2 cm), 90° twisting, and 30% lateral plus 20% longitudinal stretching. In all deformation cases, strain is concentrated at the bends and corners of the serpentine PI/Cu interconnects, with a peak principal strain of ~0.04, while the regions hosting functional components remain largely strain-isolated. Therefore, strain remains concentrated in the serpentine interconnects, while the functional islands experience much lower strain.[48] To assess on-body conformability, the integrated patch was applied directly to the wrist. Under bending, twisting, and skin stretch associated with joint motion, it remained conformally attached to the doubly curved wrist surface without visible lift-off or local misfit.

To assess the influence of circuit deformation on pressure readout, we cyclically bent or stretched the readout circuit while keeping the sensor unloaded or under a constant pressure of 50 kPa. Holding the sensor load fixed allowed changes associated with circuit motion to be assessed separately from the response to pressure. At a bending radius of ~2 cm, the unloaded signal remained close to its baseline in the unbent state (**Fig. 4b**). Applying 50 kPa raised the output, and this loaded level was maintained under the same cyclic bending conditions (**Fig. 4c**). The agreement between bent and unbent readings at both pressure levels indicates that bending affected neither the baseline nor the static pressure response to an appreciable extent. Cyclic stretching

likewise left both output levels stable (**Fig. 4d**), showing that the readout was also maintained as the circuit underwent tensile deformation.

We then combined cyclic pressure loading with circuit stretching to examine acquisition under a dynamic pressure. The sensing module was fixed on a rigid platform and cyclically compressed to a peak pressure of 50 kPa at the speeds of 1 and 3mm min^{-1}. At the same time, a movable stage applied approximately 10 cycles of lateral stretching to the readout circuit, reaching 30% strain in each cycle (**Fig. 4e**). At each compression speed, successive pressure cycles produced repeatable responses, with no apparent baseline drift during circuit stretching (**Fig. 4f).** The repeatability of the pressure responses and the stable baseline show that acquisition was maintained throughout the combined loading cycles, confirming that the compliant readout remains electrically stable under deformation and does not interfere with pressure acquisition.

The stable electrical readout under deformation mainly results from two aspects. On the one hand, the serpentine PI/Cu interconnects accommodate the relative displacement of the islands without a substantial increase in resistance. Under cyclic loading, the interconnect resistance was 7.4 Ω at 30% strain, close to its initial value of 7.0 Ω, and increased to only 9.7 Ω at 60% strain, maintaining good electrical continuity (**Fig. S13**). On the other hand, the electronic components were firmly soldered onto pads on the functional islands (**Fig. 3d**, right). The islands provide local mechanical support around the soldered connections and reduce deformation in these regions. This distribution of deformation is consistent with the FEA results, which place higher

strains in the serpentine interconnects and lower strains in the functional islands (**Fig. 4a**).

Breathability is evaluated using an evaporation test (25 °C, about 35% RH) with vials sealed by Ecoflex film, TPU fiber sheet, and patterned Ecoflex/TPU fiber layer (**Fig. S14**). Ecoflex alone shows negligible water loss over 7 days, whereas the patterned composite enables about 15% mass loss, evidencing improved vapor transport through the porous network (**Fig. 4g)**. A 48-h skin-contact test showed no visible signs of irritation, consistent with the patch's breathable and skin-compatible interface, supporting the compatibility and suitability of the FMWP for extended wear. (**Fig. 4h)**. In addition, the laminated interface also provided sufficient inherent tack to maintain stable skin-mounted attachment, and the patch remained in place when the forearm was held vertically at a 90° orientation without detachment (**Fig. 4i)**.

Overall, the integrated architecture delivers motion-robust readout with a breathable, skin-compatible interface, enabling stable long-term epidermal monitoring.

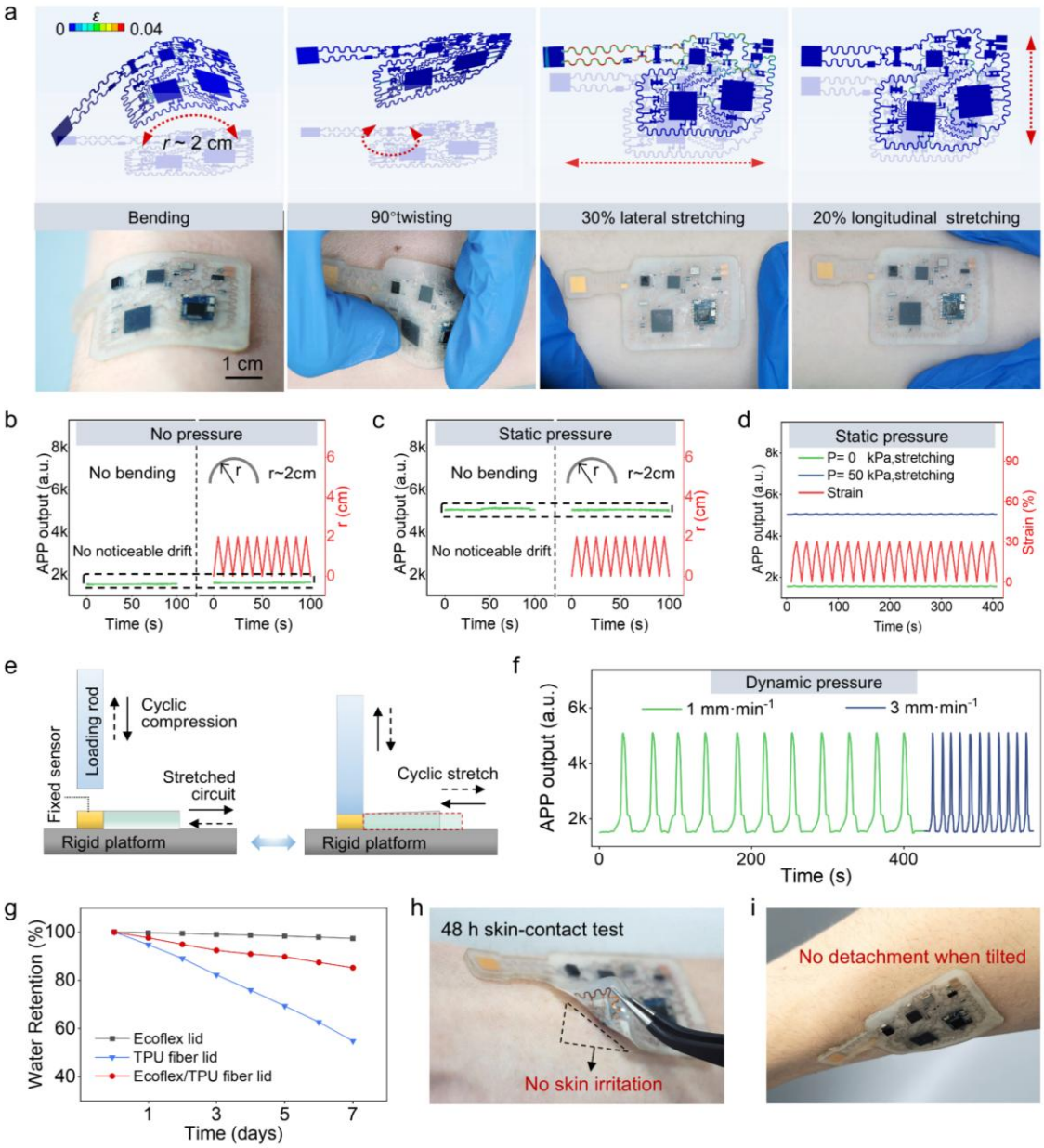


Fig. 4 Mechanical robustness, deformation-resilient signal acquisition, and skin-mounted reliability. a. FEA simulations and corresponding photographs of the FMWP under bending R ~ 2 cm, 90° torsion, 30% lateral stretching, and 20% longitudinal stretching. **b**. Wireless outputs at 0 kPa with the backend circuit in flat and bent configurations **c**. Wireless outputs at 50 kPa with the backend circuit in flat and bent configurations. **d.** Output stability during 20 cycles of 30% backend stretching at 0 and 50 kPa. **e.** Schematic of the anti-interference test. The sensor was mounted on a rigid platform and subjected to cyclic normal loading peak pressure: 50 kPa at different loading rates, while the backend circuitry was periodically deformed by a horizontally reciprocating motorized platform. **f.** Output signals during the anti-interference test. **g** Air permeability assessed

by remaining water mass over time for three sealing materials: Ecoflex, TPU fiber, and an Ecoflex/TPU fiber layer. **h**. Skin compatibility of the FMWP after 48 h continuous wear, showing no visible redness or irritation at the attachment site. **i**. Demonstration of the adhesion of the FMWP on skin, showing no detachment when the skin was tilted to ~ 90°.

Physiological Signal Monitoring by the FMWP

The untethered system integrates the iontronic sensing front end, a flexible acquisition and processing module, an onboard battery, and a Bluetooth enabled smartphone application for real-time visualization (**Fig. 5a**). The capacitance signal is digitized by an FDC2214 based LC resonance readout and transmitted at approximately 45 Hz, enabling continuous waveform streaming for subsequent time frequency analysis. The data are then wirelessly transmitted to a smartphone through a Bluetooth link for real-time visualization in a custom mobile app. To assess general applicability across representative physiological scenarios, we conducted on-body measurements at the wrist, chest, abdomen, and throat, targeting pulse, cardiopulmonary activity, respiration, and swallowing, respectively (**Fig. 5b–m**). With the patch attached to the wrist (**Fig. 5b**), the FMWP continuously captured pulse waveforms, which were displayed in real-time on the smartphone app (**Fig. 5c** and **Video S1**). The enlarged segment shows distinct, repeatable peaks, and the wavelet time–frequency map reveals a dominant component at 1.31 Hz, corresponding to a pulse rate of ~78.6 beats per minute (**Fig. 5d**).

When placed on the chest, the patch recorded a mixed cardiopulmonary waveform in which respiration-driven low-frequency deformation is superimposed with heartbeat-

related microvibrations (**Fig. 5e,f**). Wavelet analysis resolves two dominant components at 0.30 Hz and 1.11 Hz (**Fig. 5g**), corresponding to a respiratory rate (RR) of ~18 breaths per minute and a heart rate (HR) of ~66.6 beats per minute, respectively, thereby separating respiratory and cardiac signatures from the same mechanical readout. Notably, respiration can also be monitored at the abdomen (**Fig. 5h**). Compared with the chest, abdominal placement suppresses cardiac interference due to the larger distance from the heart and emphasizes breathing-driven abdominal motion (**Fig. 5i**). Accordingly, the wavelet map shows a single prominent component at 0.22 Hz (**Fig. 5j**), corresponding to an RR of ~13.2 breaths per minute. Taken together, the chest offers a convenient single-site solution for concurrent HR/RR tracking after time–frequency decoupling, whereas the abdomen provides a cleaner respiration-dominant readout that can be preferable for robust RR monitoring.

Swallowing monitoring is relevant to dysphagia screening or assessment, as impaired neuromuscular coordination can alter the timing, strength, and sequence of swallowing-related mechanical signatures.[49] With the patch applied to the throat (**Fig. 5k**), the recorded waveform showed a clear swallowing-related mechanical signature without interruption during water ingestion. The recorded signals and time–frequency indicate smooth swallowing without choking or interruption (**Fig. 5l,m** and **Video S2**), consistent with normal swallowing function. In addition, the system can wirelessly stream a range of movement-associated signals for real-time display, including wrist, elbow, and knee flexion, as well as mouth opening/closing, abnormal blinking events, and laryngeal articulation (**Fig. S15**).

Collectively, the integrated FMWP provides motion robust, real-time multi parameter physiological readout with phone connectivity, supported by a high linearity iontronic sensor, a deformation-tolerant backend circuit architecture, and a breathable skin interface for stable, long-term epidermal monitoring.

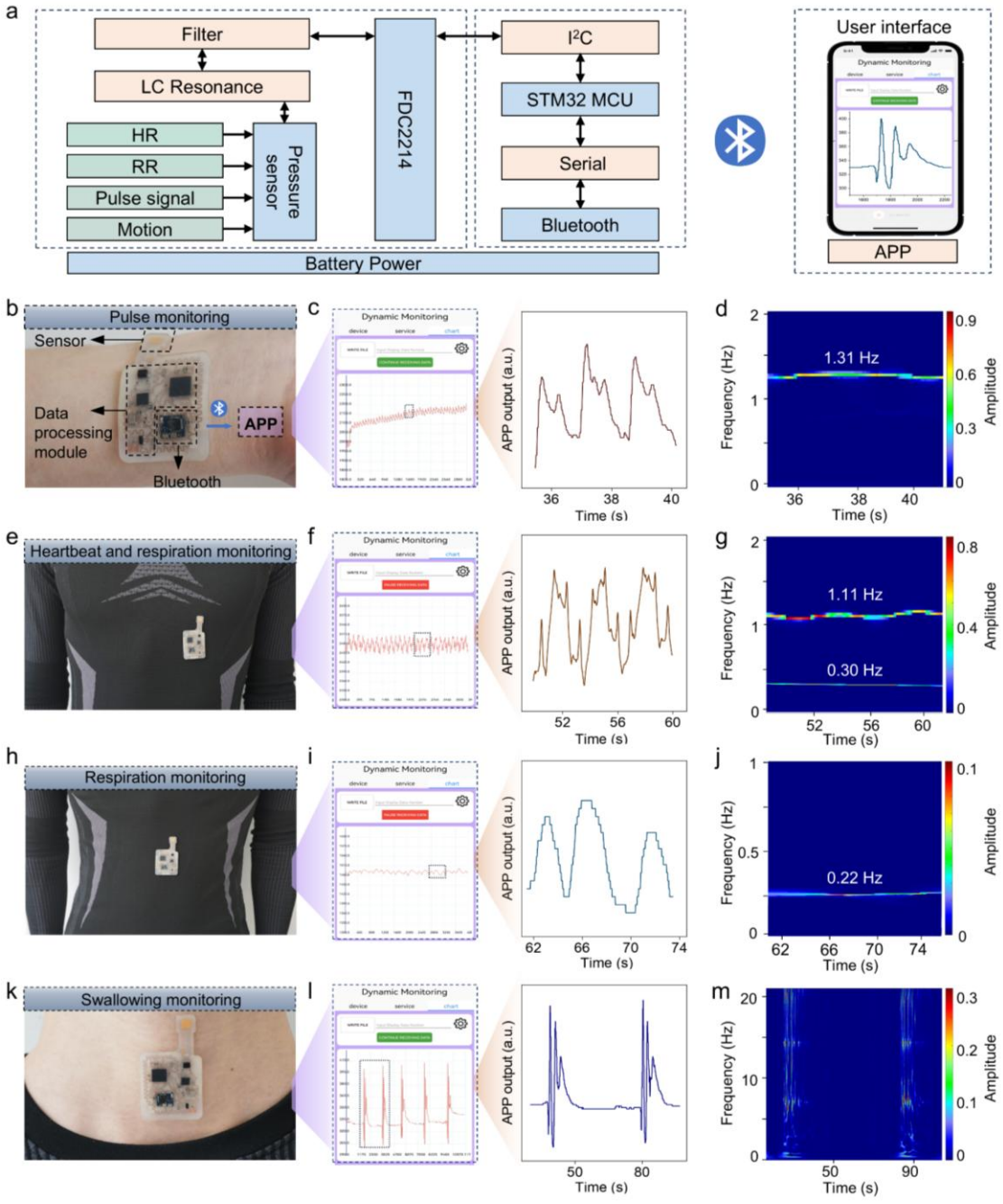


Fig. 5 Physiological signal monitoring by the FMWP. a Functional block diagram of signal acquisition and processing in the FMWP, including signal conditioning, control, wireless communication, and app visualization. **b** Photograph of the FMWP attached to the wrist. **c** Pulse

waveform shown in the app with an enlarged segment. **d** Wavelet transform map of the enlarged pulse segment in **c**. **e** Photograph of the FMWP attached to the chest. **f** Respiratory and cardiac waveforms shown in the app with an enlarged segment. **g** Wavelet transform map of the enlarged respiratory and cardiac segment in **f**. **h** Photograph of the FMWP attached to the abdomen. **i** Respiratory waveform shown in the app with an enlarged segment. **j** Wavelet transform map of the enlarged respiratory segment in **i**. **k** Photograph of the FMWP attached to the throat. **l** Swallowing waveform shown in the app with an enlarged segment. **m** Wavelet transform map of the enlarged swallowing segment in **l**.

Discussion

The iontronic pressure response is governed by pressure dependent evolution of the microstructured ionic interface from partial contact to increased effective contact area. The characteristic feature size and its dispersion strongly shape this process (**Fig. S16**). Larger features preserve deformation volume at elevated loads and delay geometric saturation, thereby broadening the linear regime (**Fig. S17**). By contrast, smaller and more uniform features compress more synchronously and reach saturation earlier; contact area growth is suppressed at high pressures and linearity deteriorates. The double-sided irregular microstructure further supports progressive engagement from both interfaces, sustaining a near-proportional increase in effective contact area across the working range. Thus, feature size and its distribution provide a way to tune the sensitivity and linear range of the sensor while retaining a scalable templating process..

For epidermal physiological signal monitoring, signal fidelity is further constrained by mounting variability and motion-coupled artifacts. A quadrant-grid spacer suppresses unintended preload contact to stabilize the initial capacitance and promotes rapid elastic recovery after unloading, supporting fast response and relaxation together

with stable cycling. To retain this device-level behavior during real wear, the backend adopts a mechanically informed island–bridge architecture. Rigid electronic islands localize strain-sensitive components in low strain regions, while serpentine PI/Cu interconnects accommodate bending, twisting, and stretching to reduce deformation-induced parasitic variations in the readout. A porous fibrous interface enables conformal skin contact while maintaining breathability during daily wear. Together, the sensor, readout circuit, and skin interface maintain stable signal acquisition during deformation and daily wear.

Methods

Finite Element Analysis

FEA was performed in ABAQUS 2022. The CNT-doped and CNT-free DSIS ionic films were modeled as nearly incompressible Mooney–Rivlin hyperelastic solids, with effective Young's moduli of 48 and 30 MPa, respectively. All contacts were defined as frictionless, with hard contact in the normal direction to prevent interpenetration. The initial electrode/ionic film contact area was evaluated under a nominal pressure of ~50 Pa. For single-sided microstructures, the bottom edges were fixed and a rigid plate was displaced downward to compress the top surface. For double-sided microstructures, the bottom rigid plate was fixed while the top plate was progressively displaced downward; lateral motion was constrained to minimize interfacial slip during compression. Hybrid elements (e.g., C3D8H) were used to alleviate volumetric locking, and the PI/Cu electrodes were simplified as rigid plates.

Preparation of Ionic Layer

The composite ionic gel solution was prepared by dissolving 1 g TPU (Mw ~ 100,000, from BASF SE) powder in 15 g N, N-dimethylformamide (99.5%, from Shanghai Macklin Biochemical Co., Ltd.) within a reagent bottle, followed by the addition of 0.7 g [EMIM][TFSI] (97%, from Aladdin Industrial Corporation). The mixture was magnetically stirred at 110°C with 1000 rpm rotation for 2 h until complete TPU dissolution. Subsequently, 0.03 g CNTs (99%, from Suiheng Technology) were added and stirred for 30 minutes. The solution was then transferred to an ultrasonic cell disruptor for 2-hour dispersion at 90 W power to ensure homogeneous CNTs distribution. Finally, the solution underwent 5-minute degassing in an ultrasonic cleaner to eliminate bubbles, yielding the final composite ionic solution. Commercial sandpaper (roughness of 1000-grit and 10000-grit sandpaper, from Eagle Axe Co., Ltd.) was patterned using a UV laser cutter (YLCF65UV) to create template components: top layer (4 cm × 4 cm) and bottom layer (2.9 cm × 2.9 cm) sandpaper templates, along with a PI tape mold featuring square apertures (3 cm × 3 cm, thickness: 150 μm). The PI tape mold was affixed to a glass substrate, securing the bottom sandpaper template while maintaining planar alignment of the square aperture region. Precisely 1.42 g of the prepared composite ionic gel solution was dispensed into the PI tape aperture. The assembly was transferred to a horizontal hot plate at 80°C for 40 minutes drying in a fume hood to achieve primary curing of the ionic layer. The top sandpaper template was then aligned and firmly attached to the layer surface. The complete template underwent bilateral hot-pressing at 110°C for 3 minutes per side using a thermal press,

simultaneously imprinting sandpaper-derived microstructures on both surfaces of the ionic layer. Post-pressing, the template was returned to the fume hood for final drying before carefully peeling off the double-sided irregular sandpaper-microstructured ionic layer from the PI tape mold.

Preparation of Iontronic Pressure Sensor

The fabrication of the flexible iontronic pressure sensor mainly involved the following steps. (i) Patterned PI/Cu electrode preparation. A 50-μm-thick PI tape was laminated onto 20-μm-thick Cu foil to form the PI/Cu film, which was then patterned into square-shaped electrodes by ultraviolet laser cutting equipment (50,000 Hz, 300 mm min^{-1}, 15 cycles). After cutting, non-patterned PI/Cu regions were removed to obtain the designed electrode configuration. (ii) Ecoflex substrate/encapsulation layer formation. Ecoflex 00-30 Parts A and B were mixed (1:1, m/m) and vacuum-degassed. The mixture was then spin-coated on a glass plate at 1000 rpm for 10 s and cured at room temperature for ~2 h to obtain a uniform elastomer layer. (iii) Water-soluble tape-assisted electrode transfer printing. The patterned electrodes were picked up using a water-soluble transfer tape and then aligned onto the Ecoflex substrate pre-coated with a thin uncured Ecoflex layer (~10 μm). After gently squeegeeing to expel trapped air, the stack was cured at room temperature to secure interfacial bonding. The sacrificial tape was subsequently dissolved by immersion in deionized water, yielding electrodes integrated with the Ecoflex substrate. (iv) Spacer fabrication and device assembly. A 10-μm-thick PET adhesive film was laser-cut into quadrant-grid spacers for later use. The device was assembled in the following order: top encapsulation layer/ top electrode/spacer/ionic

layer/bottom electrode/bottom encapsulation layer. Before assembly, the bonding surfaces of the top and bottom Ecoflex encapsulation layers were plasma-treated for 30 s and immediately brought into contact under a mild pre-pressure, enabling interfacial bonding and completing encapsulation.

Fabrication of the FMWP

PI/Cu electrodes and interconnects were patterned by UV laser ablation based on the CAD layout shown in **Fig. S10**. The laser-patterned circuit was released and transferred using water-soluble transfer tape. Electronic components were then assembled by reflow soldering. After the circuit was cleaned with anhydrous ethanol, flux and solder paste were selectively applied to the component pads, followed by component placement and reflow. The assembled circuit was spray-coated with insulating varnish to passivate exposed conductive regions and prevent electrical shorting. Each sensing unit was individually encapsulated before integration with the circuit. The integrated device was subsequently encapsulated with a spin-coated Ecoflex layer cured at room temperature. Finally, a patterned porous TPU fibrous membrane was laminated onto the Ecoflex layer using partially cured Ecoflex as the bonding layer to form the skin-contact interface. The porous membrane covered the stretchable interconnects, whereas Ecoflex remained exposed around the patch perimeter and over the rigid electronic islands to provide localized skin adhesion. This patterned interface was designed to improve breathability and wearing comfort while maintaining reliable attachment to the skin.

Data availability

The data supporting the findings of this study are available within the article and its Supplementary Information. Additional data are available from the corresponding author upon reasonable request.

References

1. Gao, S. et al. Wearable technologies for assisted mobility in the real world . *Nat. Commun*. **16,** 1098 (2025).
2. Huang, X., He, Y., Shi, Y. et al. Strain-insensitive MXene-based wearable temperature patch with integrated thermoelectric cooling for continuous infant t hermal monitoring and in-situ treatment. *npj Flex Electron*. **10**, 2 (2026).
3. Sun, Y. et al. Wearable biodevices based on two-dimensional materials: fro m flexible sensors to smart integrated systems. *Nano-Micro Lett.* **17**, 10 (2025).
4. Meng, K. et al. Bioinspired wearable pulse sensors for ambulant cardiovasc ular monitoring and biometric authentication. *Adv. Funct. Mater.* **34**, 2403163 (2024).
5. Yin, Z. et al. Wearable respiratory sensors for health monitoring. *NPG Asi a Mater.* **16**, 1 (2024).
6. Baigutanova, A. et al. A continuous real-world dataset comprising wearable -based heart rate variability alongside sleep diaries. *Sci. Data* **12**, 1474 (2025).
7. Hu, Y. et al. Prolonged monitoring and risk management of hyperuricemia using interference-resistant wearable bioelectronics. *Device* **3**, 100753 (2025).
8. Wang, X. et al. Traditional chinese medicine (TCM)-inspired fully printed soft pressure sensor array with self-adaptive pressurization for highly reliable in dividualized long-term pulse diagnostics. *Adv. Mater.* **37**, 2410312 (2025).

9. Chen, R. et al. Nonlinearity synergy: an elegant strategy for realizing high-sensitivity and wide-linear-range pressure sensing. *Nat. Commun.* **14**, 6641 (2023).

10. Tian, H. et al. Hierarchical synergetic strategy for iontronic pressure sensors with high sensitivity and broad linearity range. *ACS Sensors* **10**, 2030-2037 (2025).

11. Gao, W. et al. Sea urchin-inspired rigid-soft hybrid tactile sensor with wide linear range, fast response speed, and excellent robustness. *npj Flex Electron* **10**, 1 (2026).

12. Zhao, T. et al. Pollen-shaped hierarchical structure for pressure sensors with high sensitivity in an ultrabroad linear response range. *ACS Appl. Mater. Interfaces* **12**, 55302-55311 (2020).

13. Chang, Y. et al. First decade of interfacial iontronic sensing: from droplet sensors to artificial skins. *Adv. Mater.* **33**, 200346 (2021).

14. Li, Y. et al. Flexible iontronic sensing. *Chem. Soc. Rev.* **54**, 4651-4700 (2025).

15. Wang, X, et al. Fabrication method and various application scenarios of flexible capacitive pressure sensor based on direct formation of conical structure. *Chem. Eng. J.* **496**, 15395 (2024).

16. Wang, X. et al. Flexible iontronic pressure sensing technology: advanced structural ionic layer. *Iontronics* **2**, 1 (2026).

17. Chen, Z. et al. Two-stage micropyramids enhanced flexible piezoresistive sensor for health monitoring and human–computer interaction. *ACS Appl. Mater. Interfaces* **16**, 7640-7649 (2024).

18. An, T. et al. Multi-level pyramidal microstructure-based pressure sensors with high sensitivity and wide linear range for healthcare monitoring. *ACS Sensors* **9**, 726-735 (2024).

19. Lu, P. et al. Iontronic pressure sensor with high sensitivity and linear response over a wide pressure range based on soft micropillared electrodes. *Sci. Bull.* **66***,* 1091-1100 (2021).

20. Luo, Z. et al. High-resolution and high-sensitivity flexible capacitive pressure sensors enhanced by a transferable electrode array and a micropillar–PVDF film. *ACS Appl. Mater. Interfaces* **13**, 7635-7649 (2021).

21. Tang, J. et al. UltraHigh-transparency and pressure-sensitive iontronic device for tactile intelligence. *npj Flex. Electron.* **6**, 54 (2022).

22. Cui, X. et al. Synergistically microstructured flexible pressure sensors with high sensitivity and ultrawide linear range for full-range human physiological monitoring. *Adv. Mater. Technol.* **8**, 220060 (2023).

23. Wang, S. et al. Flexible pressure sensors with ultrahigh stress tolerance enabled by periodic microslits. *Microsyst. Nanoeng.* **10**, 2 (2024).

24. Bai, N. et al. Graded intrafillable architecture-based iontronic pressure sens or with ultra-broad-range high sensitivity. *Nat. Commun.* **11**, 20 (2020).

25. Xiao, Y. et al. Multilayer double-sided microstructured flexible iontronic pressure sensor with a record-wide linear working range. *ACS Sensors.* **6**, 1785-1795 (2021).

26. Huang, J. et al. Multi-hierarchical microstructures boosted linearity of flexib le capacitive pressure sensor. *Adv. Eng. Mater.* **24**, 210176 (2022).

27. Bai, N. et al. Graded interlocks for iontronic pressure sensors with high se nsitivity and high linearity over a broad range. *ACS Nano* **16**, 4338-4347 (202 2).

28. Yang, Z. et al. Microbubble-based fabrication of resilient porous ionogels f or high-sensitivity pressure sensors. *Microsyst. Nanoeng.* **10**, 17 (2024).

29. Liu, Q. et al. High-porosity foam-based iontronic pressure sensor with superhigh sensitivity of 9280 kPa^{-1}. *Nano-Micro Lett.* **14**, 2 (2022).

30. Liu, Y. et al. Ultrasensitive iontronic pressure sensor based on rose-structured ionogel dielectric layer and compressively porous electrodes. *Adv. Compos. Hybrid Mater.* **6**, 210 (2023).

31. Li, C. et al. Polyelectrolyte elastomer-based ionotronic sensors with multi-mode sensing capabilities via multi-material 3D printing. *Nat. Commun.* **14**, 4853 (2023).

32. Odent, J. et al. 3D-printed stacked ionic assemblies for iontronic touch sensors. *Adv. Funct. Mater.* **33**, 221048 (2023).

33. Yang, R. et al. Iontronic pressure sensor with high sensitivity over ultra-broad linear range enabled by laser-induced gradient micro-pyramids. *Nat. Commun.* **14**, 290 (2023).

34. Li, K. et al. Flexible capacitive pressure sensor with chemically reduced graphene oxide on a pyramid-structured melamine sponge array by laser engraving. *J. Mater. Chem. C* **13**, 21215-21226 (2025).

35. Li, J. et al. Thin, soft, wearable system for continuous wireless monitoring of artery blood pressure. *Nat. Commun.* **14**, 5009 (2023).

36. He, X. et al. Sweat-powered, skin-adhesive multimodal sensor for long-term and real-time sweat monitoring. *BMEMat.* **3**, e1212 (2025).

37. Wang, C. et al. High-saline-enabled hydrophobic homogeneous cross-linking for extremely soft, tough, and stretchable conductive hydrogels as high-sensitive strain sensors. *ACS Nano* **17**, 23194-23206 (2023).

38. Li, Y. et al. An ultrastretchable and multifunctional hydrophobic/electrostatic dual-crosslinked hydrogel for self-healing flexible touch panel and sensor. *npj Flex. Electron.* **9**, 4 (2025).

39. Shen, J. et al. Highly robust and fatigue-resistant organic hydrogel composite elastomer fibers with multi-sensing capabilities. *Sci. China Mater.* **68**, 4534-4545 (2025).

40. Wang, Y., Sun, C. & Ahmed, D. A smart acoustic textile for health monitoring. *Nat. Electron.* **8**, 485-495 (2025).

41. Papaefstathiou, M., Elgendi, M. & Menon, C. Balancing sensitivity and integration in capacitive pressure sensors for textile-based health monitoring. *npj Biosens.* **2**, 40 (2025).

42. Peng, Y. et al. Switchable pseudo-triaxial structure enabled mechanosensory textiles with ultra-wide detection range for flexible e-wearables. *Adv. Funct. Mater.* **34**, 241117 (2024).

43. Yuan, H. et al. Ultra-stable, waterproof and self-healing serpentine stretchable conductors based on WPU sheath-wrapped conductive yarn for stretchable i nterconnects and wearable heaters. *Chem. Eng. J.* **473**, 14525 (2023).

44. Yin, F. et al. A waterproof and breathable cotton/rGO/CNT composite for constructing a layer-by-layer structured multifunctional flexible sensor. *Nano Res.* **15**, 9341-9351 (2022).

45. Shi, S. et al. Low-density polyethylene-multi-walled carbon nanotube nanocomposite membranes with enhanced conductivity for highly sensitive vapor sensing. *Adv. Compos. Hybrid Mater.* **6**, 168 (2023).

46. Mannsfeld, S. C. B. et al. Highly sensitive flexible pressure sensors with microstructured rubber dielectric layers. *Nat. Mater.* **9**, 859-864 (2010).

47. Bai, N. et al. A robotic sensory system with high spatiotemporal resolution for texture recognition. *Nat. Commun.* **14**, 7121 (2023).

48. Kim, D-H. et al. Stretchable, curvilinear electronics based on inorganic materials. *Adv. Mater.* **22**, 2108-2124 (2010).

49. Rafeeqi, T. et al. Wearable, epidermal devices for assessment of swallowing function. *npj Flex. Electron.* **7**, 52 (2023).

Acknowledgements

This work was supported by the National Natural Science Foundation of China (Grant Nos. 52375573 and 52403335), the Natural Science Basic Research Program of Shaanxi Province (Youth Program, Category B; Grant No. 2026JC-YXQN-160), the Qinchuangyuan High-Level Innovation and Entrepreneurship Talent Program of Shaanxi Province, and the Sanqin Talent Introduction Program of Shaanxi Province.

Author information

Corresponding Authors

Weidong Wang – School of Mechano-Electronic Engineering, Xidian University, Xi'an 710071, P.R. China; State Key Laboratory of Electromechanical Integrated Manufacturing of High-Performance Electronic Equipment, Xi'an 710071, P.R. China; Email: wangwd@mail.xidian.edu.cn

Ningning Bai – School of Mechano-Electronic Engineering, Xidian University, Xi'an 710071, P.R. China; State Key Laboratory of Electromechanical Integrated Manufacturing of High-Performance Electronic Equipment, Xi'an 710071, P.R. China; Email: nnbai@xidian.edu.cn

Authors

Zhuang Su – School of Mechano-Electronic Engineering, Xidian University, Xi'an 710071, P.R. China

Chengxi Guo – School of Mechano-Electronic Engineering, Xidian University, Xi'an 710071, P.R. China

Linxuan Zhou – School of Mechano-Electronic Engineering, Xidian University, Xi'an 710071, P.R. China

Ke Liu – School of Mechano-Electronic Engineering, Xidian University, Xi'an 710071, P.R. China

Xi Wang – School of Mechano-Electronic Engineering, Xidian University, Xi'an 710071, P.R. China

Ran Zhang – School of Mechano-Electronic Engineering, Xidian University, Xi'an 710071, P.R. China

Bo Teng – School of Mechano-Electronic Engineering, Xidian University, Xi'an 710071, P.R. China

Hongcheng Xu – School of Instrument Science and Technology, Xi'an Jiaotong University, Xi'an 710049, P.R. China

Chuan Fei Guo – Department of Materials Science and Engineering, Southern University of Science and Technology, Shenzhen 518055, P.R. China

Author Contributions

Z.S. and C.G. contributed to validation, investigation, writing the original draft and visualization. L.Z. contributed to conceptualization, methodology and investigation. K.L. contributed to methodology, validation, investigation and visualization. X. W.

contributed to conceptualization, methodology and investigation. R.Z. contributed to supervision, review and editing. B.T. contributed to supervision, review and editing. H.X. and C.F.G. contributed to conceptualization, supervision, review and editing. W.W and N.B. contributed to conceptualization, supervision, funding acquisition, writing the original draft, review and editing..

[#](Z.S. and C.G.) These authors contributed equally.

Competing interests

The authors declare no competing financial interest.

Supplementary information

Supplementary information accompanies the manuscript on the npj flexible electronics website (http://www.nature.com/npjflexelectron/)

Supplementary Files

This is a list of supplementary files associated with this preprint. Click to download.

- MovieS1.mp4
- MovieS2.mp4
- SupplementaryInformation.docx
- Supplementaryfile.zip